Velocity-space resolution, entropy production, and upwind dissipation in Eulerian gyrokinetic simulations

Cite as: Phys. Plasmas **13**, 032310 (2006); https://doi.org/10.1063/1.2184069
Submitted: 17 October 2005 • Accepted: 15 February 2006 • Published Online: 29 March 2006

J. Candy and R. E. Waltz

Velocity-space resolution, entropy production, and upwind dissipation in Eulerian gyrokinetic simulations

J. Candy and R. E. Waltz
General Atomics, San Diego, California 92121

(Received 17 October 2005; accepted 15 February 2006; published online 29 March 2006)

Equations which describe the evolution of volume-averaged gyrokinetic entropy are derived and added to GYRO [J. Candy and R.E. Waltz, J. Comput. Phys. **186**, 545 (2003)], a Eulerian gyrokinetic turbulence simulation code. In particular, the creation of entropy through spatial upwind dissipation (there is zero velocity-space dissipation in GYRO) and the reduction of entropy via the production of fluctuations are monitored in detail. This new diagnostic has yielded several key confirmations of the validity of the GYRO simulations. First, fluctuations balance dissipation in the ensemble-averaged sense, thus demonstrating that turbulent GYRO simulations achieve a true statistical steady state. Second, at the standard spatial grid size, neither entropy nor energy flux is significantly changed by a 16-fold increase (from 32 to 512 grid points per cell) in the number of grid points in the two-dimensional velocity space. Third, the measured flux is invariant to an eightfold increase in the upwind dissipation coefficients. A notable conclusion is that the lack of change in entropy with grid refinement refutes the familiar but incorrect notion that Eulerian gyrokinetic codes miss important velocity-space structure. The issues of density and energy conservation and their relation to negligible second-order effects such as the parallel nonlinearity are also discussed. © *2006 American Institute of Physics*. [DOI: 10.1063/1.2184069]

I. INTRODUCTION

The connection between dissipation and statistically steady states of turbulence has been discussed by Krommes in the context of gyrokinetic and gyrofluid simulations.[1] It was demonstrated that in order to achieve a true steady state, simulations *must* include some form of dissipation. This line of reasoning leads directly to the conclusion that completely collisionless simulations are incompatible with the achievement of a turbulent steady state. The discussion in Ref. 1 is oriented toward the so-called δf method of particle-in-cell (PIC) simulation, which was (in 1994) the standard method used to simulate turbulence in gyrokinetic plasmas.

In a δf PIC simulation, the fluctuating particle distribution δf_i is proportional to the marker weight w_i, where i is a marker label. When run into the early nonlinear regime, collisionless PIC simulations generate potentials (or equivalently, fluxes) which appear to nonlinearly saturate and achieve some degree of steady-state behavior. However, at the same time, the mean-square marker weights can grow secularly,

$$\langle w_i^2 \rangle \propto t. \tag{1}$$

This troublesome statistical feature of the PIC method has been called the "growing weight problem." Further, because the fluxes appear to reach a steady state while the entropy can grow without bound,[2]

$$\text{entropy} \propto -\sum_i \langle w_i^2 \rangle \tag{2}$$

the notion of an entropy paradox was born.[1] Krommes later proposed a remedy for this problem: the so-called *W*-stat algorithm for δf simulations.[3] A *W*-stat artificially damps the weights, thereby making the realization of entropic steady states, in principle, possible. Despite this clear exposition of the problem and a potentially workable solution, the *W*-stat algorithm has not been significantly explored by the PIC community.

The issue of turbulent steady states was revisited in the context of Eulerian simulations by Watanabe *et al.*[4,5] Most recently, a detailed study of entropy balance in local Eulerian gyrokinetic simulations of the toroidal ion-temperature-gradient (ITG) mode has been reported[6] which clearly confirms the original picture developed by Krommes. In Ref. 6, nondissipative numerical methods are used, with the only dissipation arising from a physical collision operator.

In this paper we take a somewhat different approach to arrive at a similar, or at least consistent, conclusion. Specifically, we show how upwind (dissipative) advection schemes used in the GYRO code[7] naturally provide the dissipation and time irreversibilty required for the achievement of statistically steady states of turbulence. We further demonstrate that these steady states are grid converged. In doing so, we put to rest the commonplace but ill-founded notions that Eulerian simulations (a) require velocity-space dissipation (GYRO does not) and (b) miss important velocity-space structure.

The results of the present work show also that higher-order effects (in ρ_*), such as so-called parallel nonlinearity,[8–10] are quite irrelevant to the issue of entropy evolution. This observation is consistent with Refs. 3 and 4.

II. THEORETICAL FRAMEWORK

A. The gyrokinetic equation for ions

We follow here the presentation and notation of Ref. 11. We will limit our discussion to adiabatic electron dynamics and a single ion species, although the generalization to ki-

netic electrons and multiple ion species is simple. The total ion distribution, f_i, is written as a sum of an equilibrium part, F_0, and fluctuating terms,

$$f_i(\mathbf{x},\varepsilon,\mu,t) = F_0 - \frac{e}{T_i}F_0[\delta\phi(\mathbf{x},t) - \overline{\delta\phi}(\mathbf{R},t)] + h_i(\mathbf{R},\varepsilon,\mu,t). \tag{3}$$

Above, $\mathbf{x}=\mathbf{R}+\boldsymbol{\rho}$ is the particle position vector, $\boldsymbol{\rho}=\mathbf{b}\times\mathbf{v}/\Omega_{\mathrm{ci}}$ is the gyroradius vector, $\mathbf{R}$ is the guiding-center position vector, $\varepsilon=v^2/2$ is the unperturbed energy per unit mass, and $\mu \doteq v_\perp^2/(2B)$ is the magnetic moment per unit mass. Also, $\Omega_{ci}=eB/m_i$ is the ion cyclotron frequency (alternatively, the ion gyrofrequency), and m_i is the ion mass. For normalization purposes we also introduce the ion-sound speed, $c_s \doteq \sqrt{T_e/m_i}$, and the relative gyroradius, $\rho_* \doteq \rho_s/a$, where $\rho_s \doteq c_s/\Omega_{ci}$ is the ion-sound gyroradius. In Eq. (3), bars denote gyroaverages which are defined formally as

$$\bar{z}(\mathbf{R},\mathbf{v},t) \doteq \oint \frac{d\alpha}{2\pi} z(\mathbf{R}+\boldsymbol{\rho},\mathbf{v},t), \tag{4}$$

for any function, z. Note that the ion distribution as defined in Eq. (3) is expressed in terms of the particle position vector, $\mathbf{x}$, which is the quantity that appears in the Poisson and Ampère equations. However, it is often convenient to work with the total ion gyrocenter distribution, $F=F(\mathbf{R},\varepsilon,\mu,t)$. This can be obtained to first order in ρ_* by operating on Eq. (3) with $\oint d\alpha/2\pi$ to find

$$\overline{f_i} = F = F_0 + h_i. \tag{5}$$

Throughout this work, the equilibrium is assumed to be a Maxwellian,

$$F_0(\mathbf{R},\varepsilon) \doteq \frac{n_0(\mathbf{R})}{(2\pi T_i/m_i)^{3/2}} e^{-m_i\varepsilon/T_i}. \tag{6}$$

The coordinate-free form gyrokinetic equation for h_i is

$$\frac{\partial h_i}{\partial t} + (v_\parallel \mathbf{b} + \mathbf{v}_d)\cdot\nabla g_i + \mathbf{v}_E\cdot\nabla(F_0+h_i) = \mathcal{C}(h_i), \tag{7}$$

where the drift velocities are

$$\mathbf{v}_d \doteq \frac{v_\parallel^2+\mu B}{\Omega_{\mathrm{ci}}B}\mathbf{b}\times\nabla B \text{ and } \mathbf{v}_E \doteq \frac{1}{B}\mathbf{b}\times\nabla\overline{\delta\phi}. \tag{8}$$

In Eq. (7), we have introduced the nonadiabatic gyrocenter response,

$$g_i \doteq h_i + \frac{e}{T_i}F_0\overline{\delta\phi}. \tag{9}$$

We have included a collision operator C on the right-hand side of Eq. (7). In the present work, we restrict our attention to a model Krook operator only,

$$\mathcal{C}(h_i) = -\nu_{\mathrm{ii}}h_i + R(v_\parallel,\varepsilon) \tag{10}$$

where ν_{ii} is the effective ion-ion collision frequency, and R is a restoring term computed at run time to enforce exact number, momentum, and energy conservation for a given simulation resolution. The continuum limit of R is given in Eq. (6) of Ref. 12.

B. Field-aligned coordinates

In what follows, we will adopt the field-aligned coordinate system (α,ψ,θ) together with the Clebsch representation for the magnetic field,

$$\mathbf{B} = \nabla\alpha\times\nabla\psi \text{ such that } \alpha \doteq \varphi - \nu(\psi,\theta). \tag{11}$$

Here, φ is the toroidal angle, θ is an angle in the poloidal direction, and ψ is the poloidal flux. For general equilibria, the θ variation of ν must be computed numerically, but in (unshifted) circular geometry we have $\nu=q(\psi)\theta$. In general, the safety factor q is defined through the general conditions on ν,

$$\nu(\psi,0) = 0, \tag{12}$$

$$\nu(\psi,2\pi) = 2\pi q(\psi). \tag{13}$$

The associated real-space Jacobian is $\mathcal{J} \doteq (\nabla\alpha\times\nabla\psi\cdot\nabla\theta)^{-1}$. Periodicity conditions on functions are most clearly demonstrated by considering the following discrete Fourier representation,

$$z(\psi,\theta,\varphi) = \sum_j z_n(\psi,\theta)e^{-\mathrm{i}n\alpha} \text{ with } n = j\Delta n. \tag{14}$$

We impose the following topological requirements on the real quantity z:

(1) z is $2\pi/\Delta n$-periodic in φ for fixed ψ and θ;
(2) z is 2π-periodic in θ for fixed ψ and φ.

Note that when $\Delta n=1$, we simulate the full torus, albeit in a restricted radial domain. These conditions are enforced even for global GYRO simulations. In particular, condition 2 implies that the (complex) expansion coefficients satisfy

$$z_n(\psi,-\pi) = e^{2\pi\mathrm{i}nq(\psi)}z_n(\psi,\pi). \tag{15}$$

In this paper, we restrict our interest to local simulations, and specify the radial periodicity of expansion coefficients, $z_n(\psi,\theta)=z_n(\psi+L,\theta)$. We further remark that, in a local simulation, the Jacobian is evaluated at the central radial position, $\psi=\psi_0$, and is therefore a function of θ only: $\mathcal{J}=\mathcal{J}(\theta)$.

C. Velocity-space coordinatization and discretization

In the $(v_\parallel,\mu)$ coordinate system, the volume element is particularly simple,

$$d^3v = 2\pi B d\mu dv_\parallel, \tag{16}$$

with $\mu\in[0,\infty)$ and $v_\parallel\in(-\infty,\infty)$. However, we emphasize that GYRO does not use these coordinates. Instead, the equilibrium constants of motion (λ,ε), with $\lambda \doteq \mu/\varepsilon$, are preferred for numerical discretization. In these coordinates, the volume element is somewhat more complicated,

$$d^3v = 2\pi\sum_\sigma \frac{B d\lambda d\varepsilon}{|v_\parallel|}, \tag{17}$$

with $\varepsilon\in[0,\infty)$ and $\lambda\in[0,1/B(0)]$. Moreover, the parallel velocity is a function of the poloidal angle,

$$v_\parallel(\theta) = \sigma\sqrt{2\varepsilon[1-\lambda B(\theta)]}. \tag{18}$$

In Eqs. (17) and (18), $\sigma \doteq v_\parallel/|v_\parallel|$ is the sign of velocity. This representation facilitates a direct treatment of particle bounce points θ_b, for which $v_\parallel(\pm\theta_b)=0$. The reader is referred to Ref. 7 for more details. In the numerical integration over λ, no continuity of $h_i(\lambda)$ is assumed across the trapped-passing (TP) boundary at $\lambda_{TP}=1/B(\pi)$. Indeed, $h_i(\lambda)$ is allowed to be discontinuous there with no loss of accuracy.

D. Entropy as an integral measure

The information theoretic entropy of a discrete set of probabilities $p_1,\ldots,p_n$ is defined as

$$H \doteq -\sum_{i=1}^{n} p_i \log_2 p_i. \tag{19}$$

This quantity is frequently called the "Shannon entropy" in reference to Shannon's 1948 paper,[13] although some argue it was first introduced by Pauli (see Ref. 14 for details). In Ref. 13, Shannon also introduced a continuous analog of Eq. (19),

$$H \doteq -\int dz p(z)\ln p(z). \tag{20}$$

This form for H is commonly called the differential entropy, where, for our present purposes, we will interpret $z\in\mathbb{R}^6$ as a six-dimensional phase space. However, because Eq. (20) is not invariant with respect to coordinate transformations (and because p is not a dimensionless quantity), we find that the notion of a relative differential entropy is preferable,

$$H \doteq -\int dz p(z)\ln\frac{p(z)}{q(z)}, \tag{21}$$

where $q(z)$ is some convenient reference density. For the present paper, it is natural to choose $p\to F$, $q\to F_0$, and to let z be the guiding center phase space, so that

$$H = -\int d^3Rd^3v F\ln\frac{F}{F_0}. \tag{22}$$

This is the entropy of F relative to F_0. It corresponds to the choice made in Ref. 1, but not, for example, in Ref. 15. In the limit $h_i \ll F_0$, we have simply

$$H \sim -\frac{1}{2}\int d^3Rd^3v\frac{h_i^2}{F_0}. \tag{23}$$

E. Entropy evolution

To construct a functional describing the evolution of entropy, we multiply Eq. (7) by g_i/F_0 and integrate the result over the entire phase-space volume. The first term on the left-hand side becomes

$$\int d^3Rd^3v\frac{g_i}{F_0}\frac{\partial h_i}{\partial t} = \frac{1}{2}\frac{\partial}{\partial t}\left(\int d^3Rd^3v\frac{h_i^2}{F_0} + n_0\int d^3R\frac{e\overline{\delta\phi}}{T_i}\mathcal{L}\frac{e\overline{\delta\phi}}{T_i}\right). \tag{24}$$

Here, we have used the symbolic form of the Poisson equation,

$$n_0\mathcal{L}\frac{e\delta\phi}{T_i} = \int d^3v\overline{h_i}, \tag{25}$$

where the right-hand side is the perturbed density, and $\mathcal{L}$ is a symmetric linear operator,

$$\mathcal{L}\delta\phi \doteq \delta\phi - \overline{\delta\phi} + \frac{T_i}{T_e}(\delta\phi - \mathcal{A}\delta\phi). \tag{26}$$

The symbol $\mathcal{A}$ denotes a flux-surface average,

$$\mathcal{A}\cdot z \doteq \frac{\int d\theta d\alpha\mathcal{J}(\theta)z}{\int d\theta d\alpha\mathcal{J}(\theta)}. \tag{27}$$

We will also repeatedly make use of the identity

$$\int d^3Rd^3v z(\mathbf{R},\mathbf{v})\overline{w}(\mathbf{R},\mathbf{v}) = \int d^3Rd^3v\overline{z}(\mathbf{R},\mathbf{v})w(\mathbf{R},\mathbf{v}). \tag{28}$$

The contribution from parallel motion can be written as

$$\int d^3Rd^3v\frac{g_i}{F_0}\frac{v_\parallel}{\mathcal{J}B}\frac{\partial g_i}{\partial\theta}. \tag{29}$$

By expanding the real-space volume element as $d^3R/\mathcal{J} = d\alpha d\psi d\theta$, one can show that Eq. (29) becomes

$$2\pi\sum_\sigma\sigma\int d\lambda d\varepsilon d\psi\frac{1}{F_0}\left(\int d\theta\frac{\partial}{\partial\theta}\int d\alpha g_i^2\right) = 0. \tag{30}$$

This is evident upon noting that $(g_i)_n(g_i)_{-n}$ is 2π-periodic in θ. However, the presence of upwind dissipation in θ will leave a residual of the form

$$\int d^3Rd^3v\frac{g_i}{F_0}\mathcal{D}_\theta h_i \tag{31}$$

on the right-hand side of Eq. (7). Because the poloidal motion is advective, it is natural to use an upwind scheme to prevent the appearance of grid-scale oscillations. $\mathcal{D}_\theta$ is defined with the same sign as the collision operator C to emphasize that with respect to dissipation the two operators are analogous. We can write the continuum limit of the operator $\mathcal{D}_\theta$ in τ space, where $d\tau = d\theta/v_\parallel$, as

$$\mathcal{D}_\theta \doteq -\alpha_\theta(\Delta\tau)^3 c(\lambda,\varepsilon)\frac{\partial^4}{\partial\tau^4}. \tag{32}$$

In this expression, c is normalized to yield the usual third-order upwind scheme [see, for example, Eq. (2.78) of Ref. 16] with $\alpha_\theta=1$. Note, however, that c is a complicated function of λ (taken to be positive definite) due to the transfor-

mation $\theta \rightarrow \tau$. Because the overall normalization is proportional to the third power of the grid spacing, the magnitude of the numerical dissipation vanishes rapidly as the τ grid is refined. This ensures a correct approach to the dissipation-free continuum. The parameter α_θ can be used to adjust the overall dissipation level.

The grad-B and curvature drift terms,

$$\int d^3R d^3v \frac{g_i}{F_0} \mathbf{v}_d \cdot \nabla g_i \sim \int d^3R d^3v g_i \left[a(\psi_0, \theta) \frac{\partial g_i}{\partial \psi} + b(\psi_0, \theta) \frac{\partial g_i}{\partial \alpha} \right] = 0, \tag{33}$$

vanish by virtue of periodicity in α and ψ. This result requires certain approximations consistent with the gyrokinetic ordering, namely, $\partial g_i / \partial \psi \sim O(1)$, $\partial g_i / \partial \alpha \sim O(1)$, and $\partial g_i / \partial \theta \sim O(\rho_*)$. Further, equilibrium quantities are evaluated at the central radius, ψ_0. Although the physical terms vanish, we employ upwind dissipation in the radial direction leaving a term of the form

$$\int d^3R d^3v \frac{g_i}{F_0} \mathcal{D}_r h_i \tag{34}$$

on the right-hand side of Eq. (7). The explicit form of $\mathcal{D}_r$ is normally a fourth-order (as for $\mathcal{D}_\theta$) or sixth-order smoother to yield overall third-order or fifth-order upwind schemes, respectively. All simulations in this paper use a sixth-order form,

$$\mathcal{D}_r \doteq -\alpha_r (\Delta r)^5 c \frac{\partial^6}{\partial r^6}, \tag{35}$$

with c chosen to give the usual fifth-order upwind scheme for the radial advection $\mathbf{v}_d \cdot \nabla r \partial / \partial r$ when $\alpha_r = 1$.

Next, in order to evaluate the $\mathbf{E} \times \mathbf{B}$ drift terms, it is useful to first note the following results:

$$\mathbf{v}_E \cdot \nabla F_0 = \frac{\mathbf{B} \times \nabla \overline{\delta\phi} \cdot \nabla F_0}{B^2} \sim \frac{\partial F_0}{\partial \psi} \frac{\partial \overline{\delta\phi}}{\partial \alpha}, \tag{36}$$

$$\mathbf{v}_E \cdot \nabla h_i = \frac{\mathbf{B} \times \nabla \overline{\delta\phi} \cdot \nabla h_i}{B^2} \sim \frac{\partial h_i}{\partial \psi} \frac{\partial \overline{\delta\phi}}{\partial \alpha} - \frac{\partial h_i}{\partial \alpha} \frac{\partial \overline{\delta\phi}}{\partial \psi}, \tag{37}$$

where, again, we have computed to leading order in ρ_*. Periodicity in α and ψ guarantees that contribution from the nonlinear $\mathbf{E} \times \mathbf{B}$ motion vanishes,

$$\int d^3R d^3v \frac{g_i}{F_0} \mathbf{v}_E \cdot \nabla h_i = 0. \tag{38}$$

In fact, the GYRO discretization scheme exactly enforces this condition. The linear part of the $\mathbf{E} \times \mathbf{B}$ motion leaves a residual connected with the energy-dependent part of

$$\frac{1}{F_0} \frac{\partial F_0}{\partial \psi} = \frac{1}{n_0} \frac{\partial n_0}{\partial \psi} + \frac{1}{T_i} \frac{\partial T_i}{\partial \psi} \left(\frac{m_i \varepsilon}{T_i} - \frac{3}{2} \right). \tag{39}$$

The result is

$$\int d^3R d^3v \frac{g_i}{F_0} \mathbf{v}_E \cdot \nabla F_0 = \frac{1}{T_i^2} \frac{\partial T_i}{\partial \psi} \int d^3R \frac{\partial \delta\phi}{\partial \alpha} \int d^3v \varepsilon \overline{g_i}, \tag{40}$$

which follows from the symmetry of $\mathcal{L}$ together with periodicity in α. We can combine our results thus far into a single equation for the fluctuation of entropy,

$$\frac{\partial}{\partial t}(S + W) = F + (D_\theta + D_r + C), \tag{41}$$

where the individual quantities are defined as

$$S \doteq \frac{1}{2V} \int d^3R d^3v \frac{h_i^2}{F_0}, \tag{42}$$

$$W \doteq \frac{1}{2V} \int d^3R n_0 \frac{e \overline{\delta\phi}}{T_i} \mathcal{L} \frac{e \overline{\delta\phi}}{T_i}, \tag{43}$$

$$F \doteq \frac{1}{V} \frac{1}{T_i^2} \left(-\frac{\partial T_i}{\partial \psi} \right) \int d^3R \frac{\partial \delta\phi}{\partial \alpha} \int d^3v \varepsilon \overline{g_i}, \tag{44}$$

$$D_\theta \doteq \frac{1}{V} \int d^3R d^3v \frac{g_i}{F_0} \mathcal{D}_\theta h_i, \tag{45}$$

$$D_r \doteq \frac{1}{V} \int d^3R d^3v \frac{g_i}{F_0} \mathcal{D}_r h_i, \tag{46}$$

$$C \doteq \frac{1}{V} \int d^3R d^3v \frac{g_i}{F_0} \mathcal{C}(h_i). \tag{47}$$

We have removed the intrinsic volume and ρ_*-scaling factors from each term by introducing the normalization factor

$$V \doteq n_0 \left(\frac{c_s}{a} \right) \rho_*^2 \int d^3R. \tag{48}$$

Under normal circumstances, we expect that the quantity F is a positive number whereas the sources of dissipation—D_θ, D_r, and C—are negative. We make the further remark that there is *no velocity-space dissipation* in GYRO other than (possibly) C; the numerical dissipation in GYRO occurs only in real space and arises from the upwind operators $\mathcal{D}_\theta$ and $\mathcal{D}_r$. Typically, $|\mathcal{D}_\theta| > |\mathcal{D}_r|$.

F. Relations to physical quantities

The quantity F is closely related to the ion energy flux, Q_i. To see this, we first express the poloidal flux terms of a radial coordinate r using $q d\psi \simeq B_0 r dr$. Then, it follows that

$$F = \frac{1}{V} \int d^3R \frac{Q_i}{T_i} \frac{1}{L_T}, \tag{49}$$

where

$$\frac{1}{L_T} \doteq -\frac{1}{T_i} \frac{\partial T_i}{\partial r}. \tag{50}$$

It is useful to further relate F to the ion energy diffusivity, χ_i,

since that is normally quoted in GYRO research literature. The flux is related to the diffusivity according to

$$Q_i \doteq -n_0 \chi_i \frac{\partial T_i}{\partial r}, \tag{51}$$

so that F is written in terms of χ_i as

$$F = n_0 \left(\frac{a}{L_T}\right)^2 \frac{\chi_i}{\chi_{\mathrm{GB}}}. \tag{52}$$

Here, $\chi_{\mathrm{GB}} \doteq \rho_s^2 c_s/a$ is the gyroBohm unit of diffusivity. For simplicity and convenience, in the remaining sections we will refer to the F as the flux. This usage is not rigorously correct, as can be seen from the definition. Thus, the term is really shorthand for something like gradient-normalized flux.

Also, in what follows, we will for convenience refer to $S+W$ as the intensity. Since we typically find that $S \gg W$, it follows that the intensity, $S+W$, is roughly proportional to $-H$, the negative of the relative entropy as defined in Eq. (23).

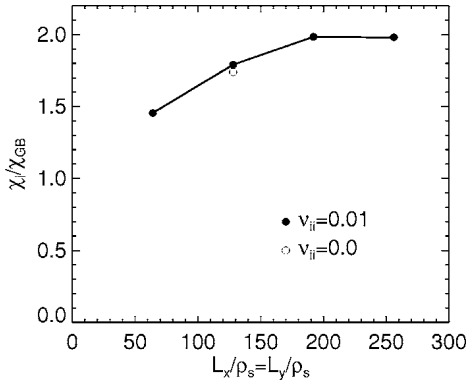

FIG. 1. Box-size scan showing approach of χ_i, as defined in Eq. (52), to the asymptotic (infinite-box) limit. The baseline resolution is used and simulations were run over the interval $0 \leqslant (c_s/a)t \leqslant 2000$. To obtain good long-time statistics, we have added a very small amount of ion-ion collisions: $(a/c_s)\nu_{ii}=0.01$. Results indicate substantial box-size convergence at $(L_x,L_y)/\rho_s=(192,192)$. An additional point (shown as an open circle) denotes a shorter, collisionless simulation over the time interval $0 \leqslant (c_s/a)t \leqslant 1000$. Points represent time averages over the interval $t \in [t_{\max}/2, t_{\max}]$.

III. NUMERICAL EXAMPLES DETAILING ENTROPY EVOLUTION

A. Nominal simulation parameters

The linear and nonlinear results presented in the body of the paper use the *cyclone base case* parameters.[17] These are $a/L_{Ti}=2.48$, $a/L_{ni}=0.8$, $R/a=2.7775$, $r/a=0.5$, $s=0.786$, $q=1.4$, and $T_e=T_i$. A simple $s-\alpha$ geometry is used with $\alpha_{\mathrm{MHD}}=0$.[7] Here, a is the plasma minor radius. All simulations, without exception, use these physical parameters.

Next, we describe a baseline numerical resolution which will serve as the starting point for all convergence studies. The baseline box size is $(L_x,L_y)/\rho_s=(128,128)$, such that $x \to r$ is the radial coordinate and $y \to \alpha$ is the second perpendicular coordinate. We have defined the box size in units of the ion-sound gyroradius, $\rho_s \doteq c_s/\Omega_{ci}$, with $c_s \doteq \sqrt{T_e/m_i}$ the ion sound speed. We use $n_x=128$ radial grid points, so that $\Delta x=\rho_s$, and $n_n=16$ complex toroidal modes such that $0 \leqslant k_y\rho_s \leqslant 0.736$. The parallel resolution is set to $n_\theta=12$ points per passing orbit (i.e., per sign of velocity). Finally, we use a 128-point velocity-space grid (8 energies, 8 pitch angles, and 2 signs of velocity). The maximum simulated energy is $\varepsilon \leqslant 5T_i/m_i$. This velocity-space resolution is typical of GYRO production runs.[18–20]

In formally collisionless simulations, published GYRO results for the cyclone base case are in very good agreement with results from the GENE,[21] PG3EQ, and GS2 codes.[22] This agreement is particularly compelling given that (a) the PG3EQ code uses the PIC method; (b) the GS2 code is a semi-implicit spectral ballooning code; (c) the GENE code is an explicit Eulerian code with velocity-space dissipation.

B. Box-size dependence

First, we wish to clarify the effect of box size on the measured ion energy diffusivity, χ_i. Figure 1 shows the effect of increasing (square) box size, and indicates that there is insignificant systematic change in χ_i past $(L_x,L_y)/\rho_s=(192,192)$. The solid points in Fig. 1 were generated by time-averaging simulations over the interval $1000 \leqslant (c_s/a)t \leqslant 2000$. These are very long time simulations (by comparison with standard production simulations) with very small ion-ion collision frequency: $(a/c_s)\nu_{\mathrm{ii}}=0.01$. This collision frequency is approximately 1/20th of a typical ITG mode frequency, $(a/c_s)\omega_{\mathrm{ITG}} \sim 0.2$. The open circle in Fig. 1 denotes the transport in our baseline (collisionless) simulation, computed by averaging over the (shorter) interval $500 \leqslant (c_s/a)t \leqslant 1000$.

The baseline box size of $(L_x,L_y)/\rho_s=(128,128)$ yields an energy flux about 10% smaller than the limiting value. Since the focus of this paper is on issues connected with grid resolution rather than on domain size, we are certain that this choice is well justified and does not affect the validity of our conclusions in any way.

C. Time dependence of flux, intensity, and dissipation

We begin our study of entropy evolution by plotting the instantaneous value of each term in Eq. (41) as a function of time. The result, shown in Fig. 2, uses parallel resolution $n_\theta=14$ (a resolution slightly greater than the baseline value of $n_\theta=12$) and finite but weak ion-ion collisions, $\nu_{\mathrm{ii}}=0.01$. Two important results are evident. First, the dominant source of dissipation arises from the parallel upwind dissipation, $\mathcal{D}_\theta$, as shown by the dotted line in Fig. 2(a). The relative contributions from radial upwind dissipation, $\mathcal{D}_r$, and collisions, $\mathcal{C}$, as plotted in Fig. 2(b), are substantially smaller. Finally, Fig. 2(c) shows that the equality in Eq. (41), which is a purely analytic result, is satisfied to high accuracy by GYRO at all times. This is an indirect check on discretization accuracy, and indicates that GYRO can be used to accurately compute higher-order moments of the perturbed distribution function. It is important to note that the changes in grid resolution and dissipation coefficients will modify the time averages of D_θ, D_r, and C, but will leave F invariant. This feature, which is a central focus of the present work, is discussed further in the subsequent sections.

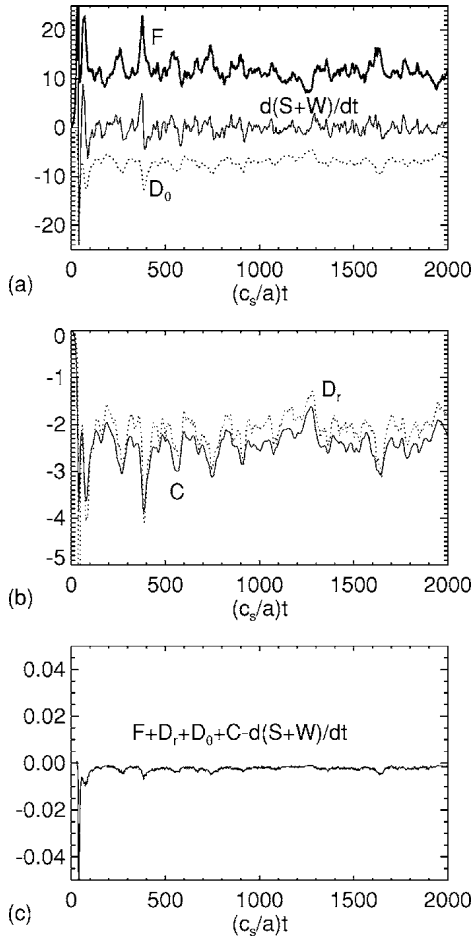

FIG. 2. Time trace of individual terms in the entropy balance equation, Eq. (41), for $n_\theta=14$ and $(a/c_s)\nu_{ii}=0.01$. Plot (a) shows the flux, F (thick solid curve); the rate of change of intensity, $\partial(S+W)/\partial t$ (thin solid curve); and the parallel dissipation rate, D_θ (dotted curve). Plot (b) shows the radial dissipation rate, D_r (dotted curve) and the collisional dissipation rate, C (solid curve). Plot (c) show the residual, which measures the accuracy to which the equality in Eq. (41) is satisfied.

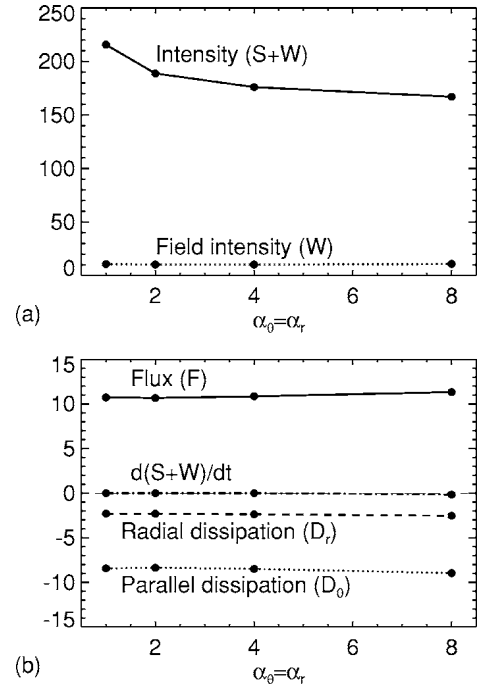

FIG. 3. Plot (a) shows the total intensity, $S+W$, as a function of the overall upwind dissipation level at fixed grid resolution. Plot (b) shows the corresponding terms in the entropy evolution equation, Eq. (41). The ion heat flux, F, is invariant to an eightfold increase in α_θ and α_r. Note that $\alpha_\theta=\alpha_r=1$ is the baseline case. All results are time averaged.

D. Effect of increasing numerical dissipation coefficients

Here, we wish to examine the sensitivity of various time-averaged quantities (flux, entropy, dissipation) to changes in the dissipation coefficients α_r and α_θ, as defined in Eqs. (32) and (35), respectively. For simplicity, we set $\alpha_r=\alpha_\theta$; that is, we take the radial dissipation coefficient, α_r, to be equal to the parallel coefficient, α_θ. We start with the baseline resolution, and work in the limit of no physical collisions ($\nu_{\mathrm{ii}}=0$). A scan over the range $1\leqslant\alpha_\theta\leqslant 8$ is shown in Fig. 3. Individual data points have been generated by averaging over $500\leqslant(c_s/a)t\leqslant 1000$. Figure 3(a) shows the only measurable effect of the variation of α_θ, namely, the total average intensity, $\langle S+W\rangle_t$, increases as the dissipation coefficients decrease. Here, $\langle\cdot\rangle_t$ denotes a time average. Since the average field intensity, $\langle W\rangle_t$, is approximately constant, we see that the entropy ($H\propto -S$) decreases slightly as the dissipation decreases. Physically, this implies that some structure in h_i that exists for $\alpha_\theta=1$ is removed at $\alpha_\theta=8$ without altering the transport properties.

Figure 3(b) illustrates the balance of energy flux and dissipation. Specifically, even though the dissipation coefficients increase by a factor of 8, the steady-state values of flux, $\langle F\rangle_t$, parallel dissipation, $\langle\mathcal{D}_\theta\rangle_t$, and radial dissipation, $\langle\mathcal{D}_r\rangle_t$, are essentially unchanged. As expected, the average rate of change of the intensity is virtually zero,

$$\left\langle \frac{\partial(S+W)}{\partial t}\right\rangle_t \sim 0, \tag{53}$$

showing that a true turbulent steady state has been achieved. In general, the length of the time record required to obtain statistically accurate averages increases with system intermittency. For the cases presented in this paper, which exhibit very little intermittency, windows of length $500(a/c_s)$ or greater appear to be sufficient. Ultimately, the results of the present scan demonstrate that the energy flux and dissipation reach a saturated level as the dissipation coefficients are increased at fixed spatial resolution.

We can probe these results more deeply by examining the spatial structure of flux. Figure 4 compares the spectral content of the energy flux for the low ($\alpha_\theta=1$) and high ($\alpha_\theta=8$) values of the dissipation coefficients. This shows that the transport acquires a slight shift to long wavelength as the dissipation coefficient increases, which can be understood intuitively as the simple preference for larger-scale structures in higher-dissipation states.

E. Invariance of results for increased velocity-space resolution

Perhaps the most important result of the present work is the demonstration that both flux and intensity are well converged with respect to velocity-space resolution at fixed spatial resolution. In Fig. 5, we plot flux and intensity for suc-

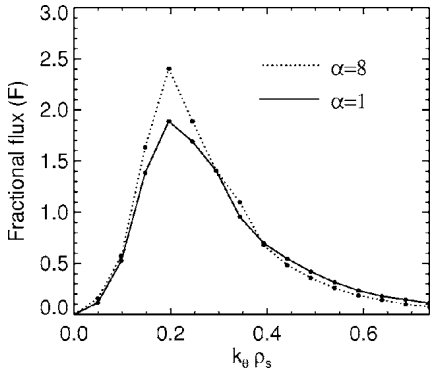

FIG. 4. Time-averaged spectral content of F for the extreme values of α_θ and α_r shown in the previous figure.

cessively finer velocity-space grids, starting from 32 grid points and moving all the way to 512 grid points. For reference, recall that the (collisionless) baseline resolution is 128 grid points. This scan shows that a 16-fold increase in the resolution changes neither the flux (which is expected based on previous GYRO convergence studies) nor the fluctuation intensity by a significant amount. The implication is that there is no missing velocity-space structure at the usual GYRO spatial resolution. Here, "missing structure" means structure that would affect either transport levels or entropy production. This result is not surprising considering that the baseline GYRO velocity-space resolution (128 velocity grid points per spatial grid point) is somewhat higher than the typical number of particles per cell (8–32) used in PIC simulations.[17,23–26]

F. Invariance of results for increased parallel grid resolution

Since most of the dissipation in the balance equation arises from D_θ, it is of interest to examine the sensitivity of individual terms in Eq. (41) to increasing parallel grid resolution, n_θ, at fixed parallel dissipation coefficient, α_θ. In GYRO, n_θ corresponds to the number of grid points (in the poloidal plane) around a passing particle orbit. Because two passing particle orbits coalesce at the trapped-passing boundary to form a pinch orbit, GYRO selects the number of points around a trapped particle orbit to be $2n_\theta$.

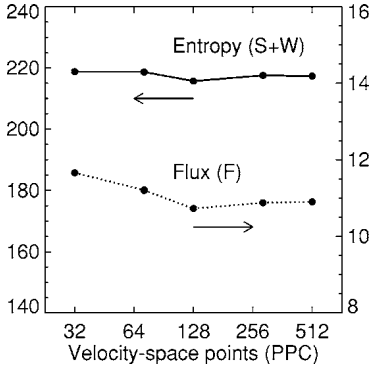

FIG. 5. Velocity-space scan, starting from low resolution (32 points) and working up to very high resolution (512 points), with the baseline case at 128 points. The upper curve (solid line) is the intensity $S+W$, and the lower curve (dotted line) is the ion heat flux. The results suggest that the baseline velocity-space resolution is more than adequate, and no significant fine structure in velocity-space develops.

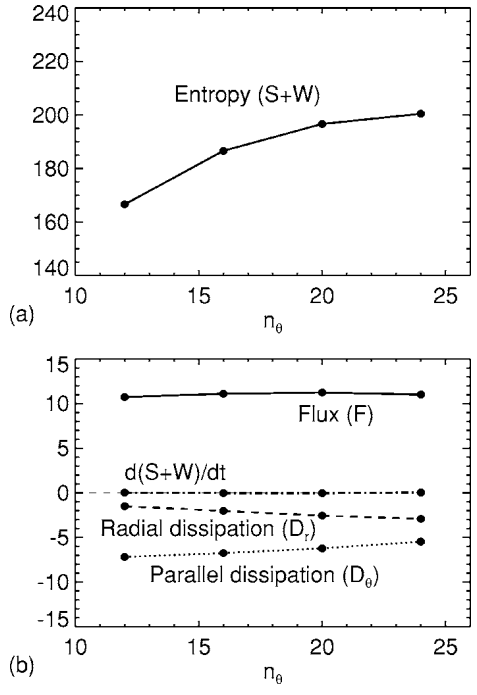

FIG. 6. Plot (a) shows the intensity, $S+W$, as a function of the poloidal grid resolution. The intensity appears to saturate at $n_\theta=24$. However, plot (b) shows that the flux, F, is already converged by $n_\theta=12$.

In Fig. 6(a) we plot the time-averaged value of the fluctuation intensity, $S+W$, as a function of the parallel resolution over the range $12 \leqslant n_\theta \leqslant 24$. The result is that the asymptotic value for $S+W$ is reached only at the relatively large value $n_\theta \simeq 24$. In Fig. 6(b), we plot the corresponding time-averaged values of the all terms in the balance equation, Eq. (41). In contrast to the intensity, here we see that the flux, F, is unchanging over the range $12 \leqslant n_\theta \leqslant 24$—despite the fact that the total parallel dissipation is decreasing (in magnitude). This feature of the simulations reinforces an important point, namely, that the details of the microscopic processes (the dissipation scale and mechanism) can change without altering the macroscopic observable (flux). This feature of the simulation, which is structurally similar to that shown in Fig. 3, is in fact a resolution of the entropy paradox.

G. Collisionless damping of zonal flows

It is of interest to make a more detailed examination of the effect of the dissipation operator $\mathcal{D}_\theta$ on the collisionless damping of zonal flows. In Fig. 7, we plot the linear $n=0$ response to an initial perturbation with $k_x\rho_s=0.1715$ (compare with Ref. 6). The solid curve shows the result using the baseline resolution, including upwind dissipation. The dashed curve shows the same computation with much higher velocity-space resolution (2048 points) and no dissipation; this is in some sense the "exact" result. The trend in the solid curve at late time indicates that phase mixing is no longer being simulated correctly for $(c_s/a)t > 45$. Two essential features of this result should be noted. First, the recurrence

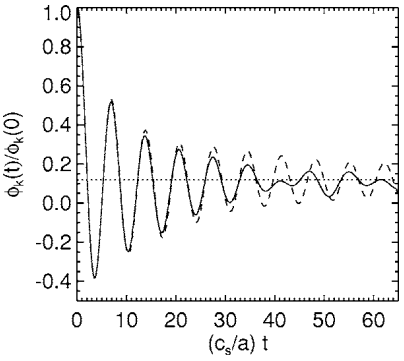

FIG. 7. Linear $n=0$ response to an initial perturbation with $k_x\rho_s=0.1715$. The solid curve shows the result using the baseline resolution, including upwind dissipation. The dashed curve shows the same computation with a 2048-point velocity-space grid and no dissipation. The late-time deviation in this case has no discernible impact on nonlinear simulations.

which would occur for $(c_s/a)t>45$ is suppressed, as expected, by the presence of $\mathcal{D}_\theta$ without significantly affecting the early-time dynamics. Second, the accuracy of the baseline resolution is actually very good up to the recurrence time, and the Rosenbluth-Hinton residual is properly recovered. In light of the previous nonlinear results, this linear test shows that the detailed phase-mixing process must only be followed accurately for a relatively short time in order for the nonlinear results to be grid converged.

IV. GYROKINETIC CONSERVATION LAWS

At this point we make a theoretical digression and discuss the issue of gyrokinetic conservation laws. The notion of order of accuracy is critical here. The theoretical literature connected with the Lie transform approach to gyrokinetic theory gives substantial attention to gyrokinetic energy conservation.[27–31] Moreover, density and energy conservation are purported to be useful diagnostics for global PIC simulations.[10,26,32–34] In what follows, we show that total density and energy are conserved to machine precision in local GYRO simulations. This means that a piecemeal inclusion of $\mathcal{O}(\rho_*^2)$ effects is not required to conserve density or energy.

A. First-order density and energy conservation

In the context of local simulations using the formalism of Sec. II, it is straightforward to compute the ion kinetic energy. Multiply Eq. (3) by $m_i\varepsilon$ and integrate over the entire phase volume to find

$$E_k \doteq \int d^3R d^3v m_i \varepsilon F, \tag{54}$$

$$= \frac{3}{2} T_i N_i + \int d^3R d^3v m_i \varepsilon h_i. \tag{55}$$

In Eq. (55), $N_i \doteq \int d^3R n_0$ is the total number of ions in the simulation volume. Flux-tube simulations enforce a periodicity assumption in ψ [see Eq. (15)] and α, together with an additional zero-average convention for fluctuations

$$\int d\alpha d\psi h_i = \int d\alpha d\psi \delta\phi = 0. \tag{56}$$

This means that the total kinetic energy in a local GYRO simulation is (exactly) time invariant and equal to the equilibrium energy: $E_k=3N_iT_i/2$. The fluctuations, which are one order in ρ_* smaller than the equilibrium, do not contribute to the kinetic energy. A nontrivial exchange of energy between particles and waves occurs only at $\mathcal{O}(\rho_*^2)$, that is, one order smaller in ρ_* (more than 100 times smaller) than the ITG fluctuation scale. Effects of this order are not treated consistently by any existing gyrokinetic code.

The result for density conservation is similarly trivial. The total ion density, N, is invariant and equal to the equilibrium density, N_i,

$$N \doteq \int d^3R d^3v F, \tag{57}$$

$$= N_i + \int d^3R d^3v h_i, \tag{58}$$

$$= N_i. \tag{59}$$

We also caution the reader on a point related to the type of simulation domain (local versus global). In the case of local simulations of turbulence, for which one expects spatially homogeneous statistics, there is a natural separation between equilibrium, F_0 and fluctuations, h_i,

$$F = F_0 + h_i, \tag{60}$$

where the background F_0 is fixed (time independent) and defines the fixed driving gradients. In local simulations, the fluctuations automatically have zero ensemble (or equivalently, spatial) average: $\langle h_i\rangle=0$. When moving to global simulations, however, the requirement that $\langle h_i\rangle=0$ means that the development of long-wavelength, time-independent spatial variations in h_i must be prohibited.[3] This constraint can be effectively enforced in global simulations through the addition of a source in the kinetic equation. Such a source is normally included in global GYRO simulations to prevent spurious relaxation of driving gradients. For global simulation, both a source *and* dissipation are required for physical realism. The dissipation can be physical or numerical, but is a requirement for the achievement of a turbulent steady state, as explained in the Introduction. A detailed exposition of global simulation techniques, however, is beyond the scope of the present paper.

B. Conservation laws with selected second-order terms

The intrinsic complexity of the collisionless GK equations as derived by the Lie transform approach[28,30] makes them unsuitable for numerical simulation. Second-order corrections to the renormalized potential [Eq. (16), Ref. 30] as well as nonlinear effects in the Poisson equation [Eq. (22b), Ref. 30] have not to date been included in any toroidal GK codes. From the physical point of view, ion collisions clearly compete with these second-order effects and perhaps even

dominate them in tokamak plasmas. This criticism clearly applies in particular to the consideration of the so-called parallel nonlinearity,[26] which we will define shortly.

Although codes do not retain $\mathcal{O}(\rho_*^2)$ effects consistently, it is nevertheless possible to include selected $\mathcal{O}(\rho_*^2)$ terms in the kinetic equation in order to derive a conservation law for energy which allows for the exchange of energy between particles and fields. To this end, we write the GK equation in conservative form using $(\mathbf{R}, v_\parallel, \mu)$ coordinates following Beer,[12]

$$\frac{\partial(BF)}{\partial t} + \nabla \cdot (BF\dot{\mathbf{R}}) + \frac{\partial}{\partial v_\parallel}(BF\dot{v}_\parallel) = 0. \tag{61}$$

The guiding-center velocity and acceleration are

$$\dot{\mathbf{R}} \doteq v_\parallel \mathbf{b} + \mathbf{v}_d + \mathbf{v}_E, \tag{62}$$

$$\dot{v}_\parallel \doteq -\frac{e}{m_i}\mathbf{b} \cdot \nabla \overline{\delta\phi} - \mu \mathbf{b} \cdot \nabla B + v_\parallel \frac{\mathbf{v}_E \cdot \nabla B}{B}. \tag{63}$$

In writing Eq. (61) we have explicitly taken the low-β limit, with $\mathbf{v}_d$ given by Eq. (8). In this limit, we can make use of the identity $\nabla \times \mathbf{B} = B\nabla \times \mathbf{b} + \nabla B \times \mathbf{b} = 0$ to further show that the Liouville theorem is satisfied,

$$\nabla \cdot (B\dot{\mathbf{R}}) + \frac{\partial}{\partial v_\parallel}(B\dot{v}_\parallel) = 0. \tag{64}$$

We emphasize that Eq. (61) is *not* the form the GK equation solved by GYRO. Specifically, Eq. (61) differs from Eq. (7) by including the $\mathcal{O}(\rho_*^2)$ parallel nonlinearity,

$$\frac{\partial h_i}{\partial v_\parallel}\left(-\frac{e}{m_i}\mathbf{b} \cdot \nabla \overline{\delta\phi} + v_\parallel \frac{\mathbf{v}_E \cdot \nabla B}{B}\right). \tag{65}$$

Note that we have rewritten the last term in Eq. (63) in a more convenient form than in Ref. 12. Let us compute the time derivative of E_k in gyrocenter coordinates,

$$\frac{dE_k}{dt} \doteq \int d^3R d^3v m_i \varepsilon \frac{\partial F}{\partial t}, \tag{66}$$

$$= \int d^3R (2\pi d\mu dv_\parallel) m_i \left(\frac{v_\parallel^2}{2} + \mu B\right) \frac{\partial (BF)}{\partial t}. \tag{67}$$

Removing the time derivative using Eq. (61) and integrating by parts gives

$$\frac{dE_k}{dt} = -\int d^3R (2\pi d\mu dv_\parallel) e (BF\dot{\mathbf{R}}) \cdot \nabla \overline{\delta\phi}, \tag{68}$$

$$= \int d^3R (2\pi d\mu dv_\parallel) e \overline{\delta\phi}\, \nabla \cdot (BF\dot{\mathbf{R}}), \tag{69}$$

$$= -\int d^3R d^3v e \overline{\delta\phi} \frac{\partial h_i}{\partial t}. \tag{70}$$

Finally, using identity equation (28), we find a constant total energy for Eq. (61),

$$E = E_k + \frac{T_i}{2}\int d^3R n_0 \frac{e\overline{\delta\phi}}{T_i}\mathcal{L}\frac{e\overline{\delta\phi}}{T_i} = E_k + T_i V W, \tag{71}$$

where W has been defined previously in Eq. (43) in the context of entropy evolution. The conservation of density, $N = N_i$, follows directly from the conservative form of the gyrokinetic equation in this case.

An additional comment in connection with entropy is in order. If indeed one takes care to include all terms in Eq. (63) when constructing an entropy balance equation from Eq. (61), one will find added parallel nonlinearity contributions to the right-hand side of Eq. (41) which are formally one order smaller in ρ_* than the existing terms. In the absence of the dissipative operators (D_θ, D_r, C), one might imagine that the parallel nonlinearity could provide a physical mechanism to balance the flux and thereby permit a turbulent steady state to exist. Indeed, in the early days of gyrokinetic PIC simulation, a belief in the physical relevance of the parallel nonlinearity led some[8] to suggest that it should actually determine the steady-state flux, while collisions would merely enhance this flux. Clearly, this state of affairs is theoretically unlikely, because any velocity-space nonlinearity is expected to generate finer and finer scales in velocity space[3] rather than eliminate them. Not surprisingly, to date no numerical demonstration of this possibility has been presented. On the other hand, both in this paper and elsewhere[5] it has been shown that nonlinear steady-state turbulence simulations with weak dissipation (and no parallel nonlinearity) asymptote to the nondissipative limit in the absence of the parallel nonlinearity.

A final remark about the dynamical effect of the parallel nonlinearity is in order. In unpublished tests we have found that for $\rho_* < 0.015$, the effect of the parallel nonlinearity on transport is so small that it cannot be measured with statistical significance. For comparison, we note that in the core of DIII-D, one typically finds $0.002 \leqslant \rho_* \leqslant 0.006$. In a reactor, nominal values of ρ_* will be smaller still.

C. Additional results for Hamiltonian systems

If the equations of motion are strictly derived from a Hamiltonian function as in the Lie transform approach,[28] then it is straightforward to derive various conservation laws using the bracket identity,

$$\int d^3R d^3v [z,w] = 0 \quad \forall\, z,w, \tag{72}$$

together with the kinetic equation

$$\frac{\partial F}{\partial t} + [F,H] = 0. \tag{73}$$

The conservation of density is trivial,

$$\frac{dN}{dt} = \frac{\partial}{\partial t}\int d^3R d^3v F = \int d^3R d^3v [H,F] = 0. \tag{74}$$

The conservation of energy, as derived in the previous section, is also clear given that

$$\int d^3Rd^3v H[H,F] = 0 = \int d^3Rd^3v (m_i\varepsilon + e\overline{\delta\phi})\frac{\partial F}{\partial t}, \quad (75)$$

which should be compared with Eqs. (66) and (70). We remark that Brizard[29] has studied gyrokinetic energy conservation to higher order using the Poisson-bracket formulation.

Finally, it is perhaps interesting to note that other nonstandard conservation quantities, $K^{(n)}$, can now be trivially identified,

$$\frac{\partial K^{(n)}}{\partial t} \doteq \frac{\partial}{\partial t}\int d^3Rd^3v F^n = \int d^3Rd^3v [H,F^n] = 0. \quad (76)$$

We believe that the $K^{(n)}$ invariants, particularly $K^{(2)}$, could serve as straightforward yet nontrivial measures of accuracy in global PIC simulations. These might be more illuminating than monitoring E.

V. DISCUSSION AND CONCLUSIONS

In this paper, we have derived an entropy evolution equation and used it as a diagnostic for nonlinear GYRO simulations. Analysis shows that GYRO simulations reach well-defined turbulent steady states where flux balances dissipation, and the time-averaged production of entropy is zero. Further, the grid convergence of time-averaged observables (intensity, flux) has been clearly demonstrated. With regard to traditional conservation laws, we have proven that GYRO local simulations automatically conserve both density and energy to machine accuracy for all times.

In view of the results we have presented, a final remark to clarify one of the claims made in Ref. 6 is in order. There, the authors suggest that "high velocity-space resolution and negligible numerical dissipation enables one to quantitatively investigate how turbulent transport depends on weak collisionality." We agree with this statement in the present context (which tacitly assumes the use of spatial grid-scale dissipation) with the added provisos:

(1) "high velocity-space resolution" means high enough to obtain fluxes which are converged at fixed spatial resolution;
(2) "negligible numerical dissipation" means a level low enough so that fluxes are invariant to spatial grid refinement; and
(3) "weak collisionality" means weak enough so that fluxes have become largely independent of collision frequency.

To this we would add that spatial upwind schemes are ideal for providing the dissipation necessary to achieve turbulent steady states, while having negligible impact on the measured flux. This is perhaps more efficient than implementing a physical collision operator with an arbitrarily chosen collision frequency. It is well-known that in many cases, finite numerical dissipation is a physically meaningful ingredient for the proper time integration of advection equations.[16] For example, as shown in Ref. 7, the parallel dissipation operator $\mathcal{D}_\theta$ ensures a smooth decay of geodesic acoustic mode oscillations. This is the physically correct behavior, in contrast to a nondissipative numerical treatment of $n=0$ oscillations, which is subject to nonphysical recurrence in time $\tau_r \sim 1/\Delta v$, where Δv represents the parallel velocity-space resolution. Indeed, the problem of recurrence in numerical simulation of Vlasov-Poisson is rather generic and to date has received much attention. Indeed, there is a variety of techniques which are routinely used to inhibit temporal recurrence in numerical schemes. For example, when advection is treated spectrally, an outgoing-wave boundary condition approach has been developed.[35] The salient point is that finite numerical dissipation is often a physically necessary feature of advanced algorithms to simulate (physically) collisionless dynamics.

ACKNOWLEDGMENT

This work was supported by U.S. Department of Energy Grant DE-FG03-95ER54309.

[1] J. A. Krommes and G. Hu, Phys. Plasmas **1**, 3211 (1994).
[2] G. Hu and J. A. Krommes, Phys. Plasmas **1**, 863 (1994).
[3] J. A. Krommes, Phys. Plasmas **6**, 1477 (1999).
[4] T.-H. Watanabe and H. Sugama, Phys. Plasmas **9**, 3659 (2002).
[5] T.-H. Watanabe and H. Sugama, Phys. Plasmas **11**, 1476 (2004).
[6] T.-H. Watanabe and H. Sugama, *Proceedings of the 20th IAEA Fusion Energy Conference, Vilamoura, Portugal, 2004*, TH/8–3Rb (2004).
[7] J. Candy and R. E. Waltz, J. Comput. Phys. **186**, 545 (2003).
[8] W. W. Lee and W. M. Tang, Phys. Fluids **31**, 612 (1988).
[9] J. C. Kniep, J.-N. Leboeuf, and V. K. Decyk, Comput. Phys. Commun. **164**, 98 (2004).
[10] L. Villard, P. Angelino, A. Bottino, S. J. Allfrey, R. Hatzky, Y. Idomura, O. Sauter, and T. M. Tran, Plasma Phys. Controlled Fusion **46**, B51 (2004).
[11] F. L. Hinton, M. N. Rosenbluth, and R. E. Waltz, Phys. Plasmas **10**, 168 (2003).
[12] M. A. Beer and G. W. Hammett, Phys. Plasmas **3**, 4046 (1996).
[13] C. E. Shannon, Bell Syst. Tech. J. **27**, 379 (1948).
[14] J. D. H. Smith, Entropie **3**, 1 (2001).
[15] R. D. Hazeltine and S. M. Mahajan, Phys. Plasmas **11**, 5430 (2004).
[16] D. R. Durran, *Numerical Methods for Wave Equations in Geophysical Fluid Dynamics* (Springer-Verlag, New York, 1999), p. 85.
[17] A. M. Dimits, G. Bateman, M. A. Beer, B. I. Cohen, W. Dorland, G. W. Hammett, C. Kim, J. E. Kinsey, M. Kotschenreuther, A. H. Kritz, L. L. Lao, J. Mandrekas, W. M. Nevins, S. E. Parker, A. J. Redd, D. E. Shumaker, R. Sydora, and J. Weiland, Phys. Plasmas **7**, 969 (2000).
[18] C. Estrada-Mila, J. Candy, and R. E. Waltz, Phys. Plasmas **12**, 022305 (2005).
[19] J. Candy, Phys. Plasmas **12**, 072307 (2005).
[20] J. E. Kinsey, R. E. Waltz, and J. Candy, Phys. Plasmas **12**, 062302 (2005).
[21] F. Jenko, T. Dannert, and C. Angioni, Plasma Phys. Controlled Fusion **47**, B195 (2005).
[22] J. Candy, R. E. Waltz, and W. Dorland, Phys. Plasmas **11**, L25 (2004).
[23] A. M. Dimits, B. I. Cohen, N. Mattor, W. M. Nevins, D. E. Shumaker, S. E. Parker, and C. Kim, Nucl. Fusion **40**, 661 (2000).
[24] A. M. Dimits, B. I. Cohen, W. M. Nevins, and D. E. Shumaker, Nucl. Fusion **40**, 1725 (2001).
[25] Y. Chen, S. E. Parker, B. I. Cohen, A. M. Dimits, W. M. Nevins, D. Schumaker, V. K. Decyk, and J. N. Leboeuf, Nucl. Fusion **43**, 1121 (2003).
[26] L. Villard, S. J. Allfrey, A. Bottino, M. Brunetti, G. L. Falchetto, V. Grandgirard, R. Hatzky, J. Nührenberg, A. G. Peeters, O. Sauter, S. Sorge, and J. Vaclavik, Nucl. Fusion **44**, 172 (2004).
[27] D. H. E. Dubin, J. A. Krommes, C. Oberman, and W. W. Lee, Phys. Fluids **26**, 3524 (1983).
[28] A. Brizard, J. Plasma Phys. **41**, 541 (1989).
[29] A. Brizard, Phys. Fluids B **1**, 1381 (1989).

[30]T. S. Hahm, Phys. Fluids **31**, 2670 (1988).
[31]T. S. Hahm, Phys. Plasmas **3**, 4658 (1996).
[32]R. D. Sydora, V. K. Decyk, and J. M. Dawson, Plasma Phys. Controlled Fusion **38**, A281 (1996).
[33]R. Hatzky, T. M. Tran, A. Könies, R. Kleiber, and S. J. Allfrey, Phys. Plasmas **9**, 898 (2002).
[34]Y. Idomura, S. Tokuda, and Y. Kishimoto, Nucl. Fusion **43**, 234 (2003).
[35]B. Eliasson, J. Sci. Comput. **16**, 1 (2001).